

High-Frequency Gravitational Wave Search with ABRACADABRA-10 cm

Kalroë M. W. Pappas,^{*} Jessica T. Fry, Sabrina Cheng, Arianna Colón Cesaní,
Inoela Vital, Jonathan L. Ouellet, Chiara P. Salemi, and Lindley Winslow[†]
Laboratory of Nuclear Science, Massachusetts Institute of Technology, Cambridge, MA 02139

Valerie Domcke and Sung Mook Lee
Theoretical Physics Department, CERN, 1 Esplanade des Particules, CH-1211 Geneva 23, Switzerland

Joshua W. Foster
*Astrophysics Theory Department, Theory Division, Fermilab, Batavia, IL 60510, USA and
Kavli Institute for Cosmological Physics, University of Chicago, Chicago, IL 60637, USA*

Reyco Henning
*Department of Physics and Astronomy, University of North Carolina, Chapel Hill, Chapel Hill, NC, 27599 and
Triangle Universities Nuclear Laboratory, Durham, NC 27710*

Yonatan Kahn
Department of Physics, University of Toronto, Toronto, ON M5S 1A7, Canada

Nicholas L. Rodd and Benjamin R. Safdi
*Berkeley Center for Theoretical Physics, University of California, Berkeley, CA 94720 and
Theoretical Physics Group, Lawrence Berkeley National Laboratory, Berkeley, CA 94720
(Dated: May 6, 2025)*

ABRACADABRA-10 cm has had great success as a pathfinder lumped-element axion dark matter experiment, setting limits on axion dark matter at the GUT scale. Now, using the interaction of gravitational waves with electrodynamics and a change in readout strategy, we use the ABRA-10 cm detector for the first search for high-frequency gravitational waves using a modified axion detector. Potential sources at these high frequencies (10 kHz to 5 MHz) include merging primordial black hole binaries or superradiance, among other beyond the standard model phenomena. This paper presents the design, results, and challenges from the ABRA-10 cm high-frequency gravitational wave search, showing it is possible to simultaneously look for axions and high-frequency gravitational waves with both searches matching theoretical expectations for sensitivity. Additionally, we conducted the first time series transient search with data from an axion experiment, achieving sensitivity to 10^{-4} in strain. Scaled directly to the next generation axion experiment, DMRadio-GUT, this sensitivity would imply a reach to $0.01 M_{\odot}$ primordial black hole mergers at distances around 3 pc, with prospects to go significantly further with modifications to the readout.

INTRODUCTION

LIGO and other interferometry-based experiments have detected gravitational waves (GWs) with sensitivity up to around 10 kHz, which marks the highest frequency expected for known compact-object mergers [1, 2]. GWs above 10 kHz would be a smoking-gun signal of new physics, such as superradiance and primordial black hole (PBH) mergers in the later universe [3]. A PBH describes a black hole formed before matter-radiation equality. Their early formation allows PBHs to be one of the few viable non-particle candidates for dark matter (DM) [4]. A low-mass PBH merger would emit high-frequency GWs (HFGWs) during the stable in-spiral as well as during the chirp and subsequent ringdown. Interferometry-based GW detectors are generally not optimized for high-frequency, and as interest increases, new methods for searching for HFGWs are being explored with axion experiments; for a review, see Ref. [3].

The ABRACADABRA-10 cm experiment was designed as a first-of-its-kind low-mass axion detector, achieving sensitivity in the mass range of 0.3 to 8 neV, with world-leading sensitivity down to $g_{a\gamma\gamma} < 3.2 \times 10^{-11} \text{GeV}^{-1}$ [5, 6]. Ultralight axions ($m \ll 10 \text{eV}$) are a leading candidate for DM [7, 8]. Axions are expected to couple weakly to electromagnetism, causing a modification to Maxwell's equations that opens a path to detection through the small effective currents sourced in strong magnetic fields. ABRA-10 cm demonstrated a new detection technique which uses a toroidal magnet read out inductively that allowed for the search of low-mass axions ($m \ll 1 \mu\text{eV}$) [9, 10], as opposed to cavity-based experiments where the detectable axion wavelength is tied to the cavity volume [11–14], see Refs. [15–18] for recent results. The success of ABRA-10 cm followed by SHAFT [19] opened the path to a significant increase in axion sensitivity for similar instruments with upgraded hardware. To achieve this, the ABRA-10 cm and DM-

Radio Path finder experiments joined forces to realize the DMRadio program to search for GUT-Scale Axions [20–23].

In this *Letter*, we exemplify the broad power of low-mass axion haloscopes by demonstrating their ability to search for HFGWs. In particular, GWs passing through the instrument produce an electromagnetic signal analogous to the axion signal [24–26]. We call the modified ABRA-10 cm experiment for searching for HFGWs ABRA-GW. As outlined in this paper, the ABRA-GW path-finder experiment proves axion haloscopes can achieve the expected HFGW sensitivity simultaneous to an axion search, without compromising either signal. Additionally, we perform the first transient time-series base analysis with an axion experiment.

DETECTION METHOD

Both axions and GWs modify Maxwell’s equations to produce an effective current, referred to as axion [27–29] and GW [30, 31] electrodynamics, respectively. These same equations are also responsible for the Primakoff effect for axions and the analogous inverse Gertsenshtein effect [24–26] for GWs. Denoting the flat spacetime metric by $\eta_{\mu\nu}$, a GW $h_{\mu\nu}$ modifies this to $g_{\mu\nu} = \eta_{\mu\nu} + h_{\mu\nu}$ and is described by two polarizations h^+ and h^\times . The perturbation to the metric results in an effective current,

$$j_{\text{eff}}^\mu \equiv \partial_\nu \left(-\frac{1}{2} h_\alpha^\alpha F^{\mu\nu} + F^{\mu\alpha} h_\alpha^\nu - F^{\nu\alpha} h_\alpha^\mu \right). \quad (1)$$

In the presence of a large magnetic field, the GW induces a current, much like the axion.

The derivation of the GW signal in ABRA was performed in Refs. [30, 32]. At the heart of ABRA is a toroidal magnetic field. We take the toroid to have inner radius R , width a , height H , and peak field value B_{max} (see Fig. 1). Inside the toroid the DC magnetic field is azimuthal and varies with the radial distance, ρ , as $\mathbf{B}_0 = B_{\text{max}}(R/\rho)\hat{e}_\phi$. Outside, the field vanishes. The GW interacts with \mathbf{B}_0 to generate an oscillatory magnetic field at the angular frequency of the GW, ω . The induced field is determined by the Biot-Savart law,

$$\mathbf{B}_h(\mathbf{r}') = \int_{V_B} d^3\mathbf{r} \frac{\mathbf{j}_{\text{eff}}(\mathbf{r}) \times (\mathbf{r}' - \mathbf{r})}{4\pi|\mathbf{r}' - \mathbf{r}|^3}. \quad (2)$$

The integral is taken over the volume of the toroid’s magnetic field, V_B . Like the axion searches of ABRA-10 cm, we search for this induced magnetic field, oscillating with the GW frequency, as our signal.

The HFGW magnetic field can be detected from the changing magnetic flux through a pickup loop placed in center of the toroid, as shown in Fig. 1. Integrating over the pickup loop area, A_ℓ , the flux is given by

$$\Phi_h = \int_{A_\ell} d\mathbf{A}' \cdot \mathbf{B}_h(\mathbf{r}'), \quad (3)$$

which induces a current in the pickup loop that is read out with quantum current sensors. Unlike the axion, which generates an azimuthally symmetric field, the magnetic field induced by a GW has an approximately dipolar structure. This structure results in a weaker coupling to a azimuthally-symmetric pickup. Since ABRA operates in the magnetostatic limit, $\omega L \ll 1$,¹ with $L = \{R, a, H\}$ denoting the typical scales of the detector, we can expand the predicted signal in powers of ωL . For a circular pickup loop, the leading order contribution, $\mathcal{O}(\omega^2 L^2)$, cancels and the signal is exclusively sourced by the h^\times polarization [32],

$$\Phi_c = \frac{ie^{-i\omega t}}{48\sqrt{2}} h^\times \omega^3 B_{\text{max}} \pi r^2 a R (a + 2R) \sin^2 \theta_h, \quad (4)$$

where θ_h indicates the direction of the incoming GW relative to the symmetry axis of the detector. However, if a semicircular figure-8 loop (see GWC and GWP in Fig. 1) is used instead, then the dipole-structured signal is able to couple to terms up to ω^2 . The figure-8 pickup additionally couples to both the h^\times and h^+ components of polarization. The flux for a figure-8 pickup is approximated as [32]

$$\begin{aligned} \Phi_8 = & \frac{e^{-i\omega t}}{3\sqrt{2}} \omega^2 B_{\text{max}} r^3 R \ln(1 + a/R) \sin \theta_h \\ & \times (h^\times \sin \phi_h - h^+ \cos \theta_h \cos \phi_h). \end{aligned} \quad (5)$$

These equations for flux are derived in the limit that the magnet is a rectangular toroid with $H \gg a, R$. In the analysis presented here we go beyond these approximations, computing the flux on the pickup loop resulting from a GW by simulation as outlined below.

DETECTOR

ABRA-GW is designed to simultaneously look for axions and HFGWs. ABRA-GW was built as a modification to the original ABRA-10 cm axion detector [6, 35, 36], which consists of a superconducting toroidal magnet with an NbTi pickup structure inside a superconducting shield, all cooled to cryogenic temperatures. Superconducting quantum interference devices (SQUIDS) were used to detect signals in the form of small-currents in the pickup structures. The magnet, pickups, and shield are cooled to ~ 1 K and the two-stage Magnicon DC SQUIDS are cooled to ~ 800 mK using an Oxford Engineering dry dilution refrigerator. The pickup system for ABRA-GW

¹ In general, the magnet is not rigid in the presence of the GW, leading to additional induced magnetic fields of $\mathcal{O}(hB_0)$ [33, 34]. Since the ABRA pickup loop is placed in a region where $B_0 \simeq 0$, this does not affect the results presented here.

is constructed with two pickups for detection: a circular pickup for axion detection, and a semicircular figure-8 pickup for HFGW detection. To first order, the axion signal does not induce a current in the figure-8 loop, and the HFGW signal does not induce a current in the circular loop as a result of low mutual inductance between the two shapes. Through simulation with COMSOL, we found a mutual inductance of $\sim 2 \times 10^{-5}$ nH between the circular and the figure-8 pickup loops (AP and GWP in Fig. 1), as compared to ~ 30 nH between the figure-8 pickup and calibration loops (GWP and GWC in Fig. 1), and ~ 21 nH between the circular pickup and calibration loops (AP and AC in Fig. 1). This six-orders-of-magnitude difference in the mutual inductance between cross-signal measurements and same-signal measurements allows for simultaneous searches of axions and HFGWs.

The experiment was calibrated using superconducting loops of NbTi wire shaped to mimic the desired signals. For the axion signal, the original setup from the ABRA-10 cm axion searches was used, consisting of a circular loop of wire with a radius of 4.5 cm running through the center of the magnet [35]. An oscillating current is injected into the circular axion calibration loop and measured using the pickup structures. Similarly, an oscillating current is also injected into the HFGW calibration loop, which is in the shape figure-8 to mimic a HFGW signal. The HFGW calibration loop is located 1 cm above the figure-8 pickup loop. A diagram of the pickups and calibration loops inside the shield containing the magnet is shown in Fig. 1. For each calibration signal injection, data was collected for both pickup structures to measure system response and cross correlation. Calibration data was collected before and after science data collection to ensure detector stability. The calibrations provide the detector response to a one-dimensional current in the shape of the signal, but the volumetric nature of the axion and HFGW signals were studied using simulations done with COMSOL.

The effective current resulting from a HFGW in the magnet volume was input to COMSOL using the equations found in Ref. [32], with extensions to account for the finite height of the magnet. The full function for the effective current can be found in the supplementary material (SM); terms up to ω^2 were input to COMSOL in the form of external current density. The flux on the pickup resulting from the effective current was found by integrating over the surface of the pickup area.

DATA COLLECTION AND BACKGROUNDS

Data for the axion and HFGW searches were collected simultaneously in time as two constant streams. An AlazarTech 9870 8-bit digitizer [37] was used for data collection and the digitizer was locked to a Stanford Research Systems FS725 Rubidium frequency standard.

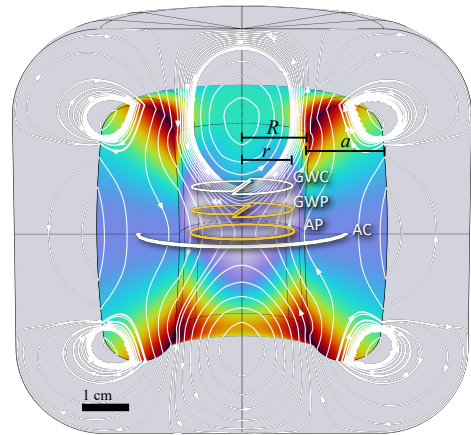


FIG. 1. Schematic of ABRA-GW for a wave entering from the right side of the figure. The magnitude of the effective HFGW current is shown as a color gradient (white/purple as smallest magnitude and black/red as the largest magnitude) in the volume of the toroidal magnet and the magnetic field lines resulting from the HFGW effective current are shown in white. The two orange loops in the center of the magnet are the axion pickup (AP) and GW pickup (GWP) and the white loops are the axion calibration loop (AC) and the GW calibration loop (GWC). The magnet width, a , is 3 cm, the inner radius, R , 3 cm, and the radius of the pickup loops, r , is 2.22 cm.

The sampling rate used was 10 MHz, giving a Nyquist frequency of 5 MHz. We used a 10 kHz high-pass and a 5 MHz low-pass physical filters to attenuate the noise at low frequencies and prevent aliasing. We collected data for six days from December 4 to 9, 2023 on both the axion and HFGW channels, with a brief break after the first few hours as a result of memory buffer issues in the data-taking computer.

The raw data contained a few distinct background signals including a 5 MHz signal and a 13 kHz signal, confirmed to exist in the data taken with both the magnet charged and uncharged. After using a Butterworth filter from 10 kHz to 3 MHz, the 13 kHz signal remained as the most prominent background in the data. The digital filtering was performed after all the data had been collected.

RESULTS

Axion Sensitivity. The axion data for the ABRA-GW search was used to determine the potential sensitivity of the setup to axions. An axion search was not performed for this paper; the data collected could be analyzed identically to Refs. [6, 35, 36, 38] to create axion limits.

The noise on the axion search was determined by comparing the axion data power spectral density (PSD) to the SQUID noise floor PSD, similar to Ref. [35]. The SQUID noise floor is defined as the output of the SQUID when there is no connected pickup loop and therefore no

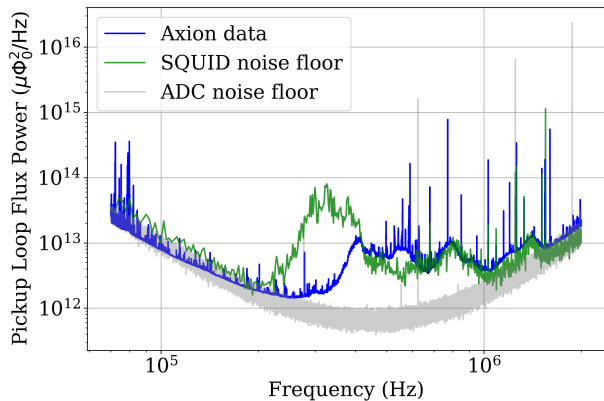


FIG. 2. Axion data collection (blue), SQUID noise floor (green), and digitizer noise floor (gray). Data shown is in power on the pickup loop, with all hardware filters divided out. There are some regions where the axion data seems to be more sensitive than the SQUID noise floor. We attribute this unlikely situation to differences in data collections periods, which were months apart and the experiment was thermal-cycled between collections. We observed that the axion data taken simultaneously with the HFGW collection had a noise floor that matched the SQUID noise floor at high frequency.

direct input to the SQUID. We demonstrate with Fig. 2 that the axion sensitivity in the region of interest (100 kHz to 2 MHz, based on Ref. [6]) was not degraded by the HFGW search. The noise features of the spectrum are similar to ones encountered in previous ABRA-10 cm campaigns, for more information on how these features are handled in an axion search see the SM of Ref. [6]. The axion data taken during six-day-long collection period is segmented, transformed to PSDs, averaged down, and compared to the SQUID noise floor. All the data shown in the figure are corrected for the shapes of the physical high and low pass filters. The calibration data was used to transform the spectra into the equivalent input at the pickup loop of the axion pickup loop. For the SQUID noise floor, we used data taken a few months prior with the same SQUID that was used for the axion data. Similarly to the ABRA-GW axion result, figure 5 of Ref. [36] shows that first axion search of ABRA-10 cm also had a noise floor close to that of the SQUID noise floor. The noise floor in Ref. [36] was determined analytically instead of experimentally, as the first axion search did not take data with the SQUID disconnected.

GW Strain Sensitivity. The strain-equivalent noise (SEN) determines how the detector noise impacts strain sensitivity. In our analysis, we assume a stationary and constant signal over the data collection period. To get the SEN, we used calibration results to convert from digitizer voltage to pickup flux, and simulation to convert flux on the pickup to strain. We use the equations for effective current from Ref. [32] as input to the simulations, and we choose the GW parameters that produce the strongest signal. These parameters describe an incoming wave at an incident angle of $\theta_h = \phi_h = \pi/2$; in this case, the

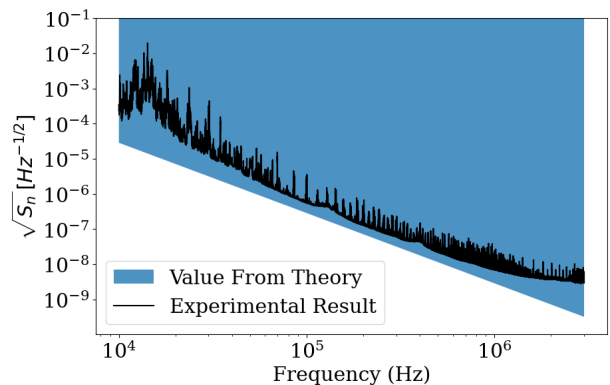


FIG. 3. Strain-equivalent noise power as theoretically estimated and as achieved by ABRA-GW. Results are purely the h^\times polarization of the strain in the angular direction which maximizes amplitude. The data was averaged over a six-day-long period.

h^\times term dominates by an order of magnitude and for simplicity we approximate the signal as purely h^\times . The theoretical calculation shown in Fig. 3 used the characteristic DC SQUID noise floor and the same parameters for the signal as were used in the simulation. The flux on the pickup was estimated using Eq. (5). More information about the experimental and theoretical calculations can be found in the SM. As can be seen in Fig. 3, the experimental result closely matches the theoretical expectation.

Transient Search. For the purposes of our demonstrator experiment, we only computed one signal template of two equal-mass PBHs ($m_1 = m_2 = 0.01 M_\odot$) with no eccentricity and a fixed sky position to use in our transient analysis. The analysis framework can be generalized to multiple templates, time and computing resources permitting. This template models the scenario where the PBH merger event is at some distance from the center of the detector. All parameters were chosen to maximize the strain in the merger within our frequency window (10 kHz to 3 MHz) and are listed in the SM. The ripple code base [39] was used to generate the waveforms of the two polarizations of strain for the merger. The amplitude of the signal scales inversely to the distance from the detector to the source. Our template models a merger event occurring 100 km from the center of mass of the detector, corresponding to strain $\mathcal{O}(10^{-4})$, as shown in the SM.

As a result of the 13 kHz background signal and other unidentified noise sources, the local mean of the GW data is non-zero and a traditional matched-filter would require a more complicated implementation for our analysis. To account for this non-zero mean we use Gaussian process modeling (GPM). Once the raw data is filtered to the same frequency range as the template (10 kHz to 3 MHz), GPM is used to construct the marginalized likelihood for the residuals. The residuals are the difference between the detector data and the signal, $\mathbf{r}(t, d) = \mathbf{d}(t, d) - \mathbf{s}(t, d)$, for a signal at distance d from the detector. The test

statistic is given by

$$TS = -2 \ln p(\mathbf{r}|t, d), \quad (6)$$

for the log-marginalized likelihood of the residuals, $\ln p(\mathbf{r}|t, d)$. For the transient search, we allow the distance to vary in each segment of data analyzed and find the smallest distance we can exclude at a 90% confidence level (CL) for that segment.

With a search window of $30 \mu\text{s}$, corresponding to the length of the signal template, we use a time step of $0.4 \mu\text{s}$ to ensure the signal won't be missed when scanning over data segments. As a demonstration, we ran the GPM analysis on a portion of the data. For a total data collection time $T = 518459 \text{ s} \simeq 144 \text{ hrs}$, we have $N_{\text{process}} = 1.29 \times 10^{12}$ total segments to process. Analyzing the full dataset is beyond the scope of this work. Instead, the path-finder analysis conducted in this paper used a 10 ms portion of the data. We tested the GPM analysis on the lowest noise period of the data (determined by power in 10 ms bins, see the SM), along with an average noise period of the data. Comparing these periods, we found that the distance which all segments within each period excluded to at least a 90% CL was similar across more and less noisy time periods. This result was expected as the noise had overall low variance over the six-day collection period, as discussed in the SM. The proof-of-principle analysis conducted here should be viewed as obtaining conservative limits; refinements could strengthen the sensitivity. In addition to improving the analysis, the next-generation of GUT-scale axion experiments, the DMRadio-GUT experiment [23] will have a sensitivity much larger than ABRA-GW. Using the results of Ref. [30], we would expect an improvement of $\simeq 2 \times 10^{12}$ in strain sensitivity from ABRA-GW to DMRadio-GUT, even with this conservative analysis. If the mechanical readout scheme of Ref. [34] were adopted, the sensitivity could be improved parametrically further still.

Out of 24975 windowed data segments searched in our pathfinder analysis, corresponding to 10 ms of collection time, all segments excluded a distance of 46.03 km (strain $\mathcal{O}(10^{-4})$) to at least a 90% CL. Given that we expect the dominant signal contribution around the merger frequency, which for $0.01 M_{\odot}$ PBHs is $f_{\text{isco}} \simeq 0.2 \text{ MHz}$, this is consistent with expectation from the strain-equivalent noise in Fig. 3: $h_{\text{sens}} \sim \sqrt{S_n f_{\text{isco}}} \simeq 4 \times 10^{-5}$. More details are given on determining this distance in the SM. If we take this result from ABRA-GW and scale it to the sensitivity of DMRadio-GUT, we would obtain a strain sensitivity of $\mathcal{O}(10^{-16})$, corresponding to distances $\mathcal{O}(1)$ parsec. Figure 4 shows the DMRadio-GUT projection for limits on the distance of the source as a function of the source position across the sky, in coordinates where the z-axis lines up with the z-axis of the instrument. Given the length of the data analyzed, there are portions of the sky to which we appear to be insensitive, however, more

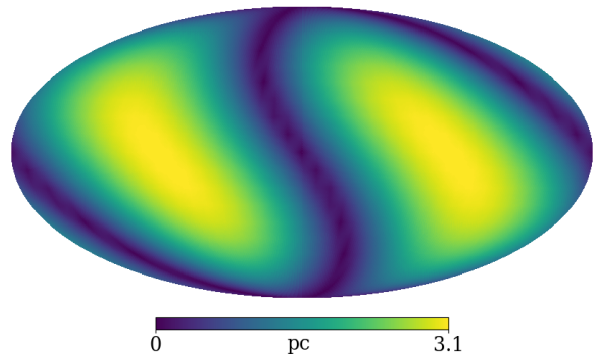


FIG. 4. Distance from detector to source for the minimum excluded amplitude found from the GPM analysis, projected for DMRadio-GUT and plotted over the sky in instrumental coordinates with the z-axis aligned with the center of the sky map.

time analyzed would allow for movement of the detector as a result of the rotation of the Earth, and we would achieve full sky coverage.

CONCLUSION

We have demonstrated the first conversion of a lumped-element axion detector to a HFGW detector and the first time-series transient search with an axion experiment. ABRA-GW achieved the predicted sensitivity to HFGW without a decrease in sensitivity to axions. Transforming the existing ABRA-10cm experiment required upgrading the hardware by designing a detector scheme with a new layout in the dilution refrigerator (which allowed for the use of two current sensors), conducting calibrations for both sensors, configuring the computer to enable data collection in two simultaneous streams, developing simulations to characterize the signal shape and the detector response to the expected signals, and developing and executing the time series analysis pipeline. Using GPM, we were able to perform a transient search over a time series data set with a non-zero mean. The sensitivity to HFGWs we achieved matches theoretical expectation, giving us the infrastructure to scale with more sensitive experiments like DMRadio-GUT which will reach down to strains $\mathcal{O}(10^{-16})$ [30].

In the coming years as haloscopes dramatically improve their axion sensitivity, these same experiments can be modified to simultaneously perform HFGW searches. These modifications broaden our searches for beyond the Standard Model physics, and more specifically to different DM candidates. Future axion experiments can greatly increase their sensitivity to HFGWs by two methods: changing their pickup geometry, as was done with ABRA-GW, and/or by using a coincidence search with multiple detectors (cf. Ref. [40]). As DMRadio-50 L [21, 22] takes its first data this year, we can utilize

the detector’s resonance-enhanced sensitivity in conjunction with ABRA-GW to perform the first HFGW coincidence search [21]. With correlated signals and uncorrelated noise, the veto power of a two-detector analysis will not only increase sensitivity to DM PBHs, but also significantly increase the sensitivity to stochastic signals and other signs of beyond-the-standard-model physics.

We would like to thank our DMRadio colleagues for useful discussions. This research was supported by the National Science Foundation under grant numbers NSF-PHY-2411650, NSF-PHY-1658693, and NSF-PHY-1806440. The research of N.L.R. was supported by the Office of High Energy Physics of the U.S. Department of Energy under contract DE-AC02-05CH11231. R.H. is supported by the US Department of Energy, Office of Science, Office of Nuclear Physics grants DEFG02-97ER41041 and DEFG02-97ER41033 B.R.S. is supported in part by the DOE award DESC0025293, and B.R.S. acknowledges support from the Alfred P. Sloan Foundation. This manuscript has been authored in part by Fermi Forward Discovery Group, LLC under Contract No. 89243024CSC000002 with the U.S. Department of Energy, Office of Science, Office of High Energy Physics.

* kaliroe@mit.edu

† lwinslow@mit.edu

- [1] N. Aggarwal, O. D. Aguiar, *et al.*, “Challenges and opportunities of gravitational-wave searches at mhz to ghz frequencies,” *Living Reviews in Relativity* **24** no. 1, (Dec., 2021) . <http://dx.doi.org/10.1007/s41114-021-00032-5>.
- [2] N. Bartolo, C. Caprini, *et al.*, “Science with the space-based interferometer lisa. iv: probing inflation with gravitational waves,” *Journal of Cosmology and Astroparticle Physics* **2016** no. 12, (Dec., 2016) 026–026. <http://dx.doi.org/10.1088/1475-7516/2016/12/026>.
- [3] N. Aggarwal *et al.*, “Challenges and Opportunities of Gravitational Wave Searches above 10 kHz,” (1, 2025) , [arXiv:2501.11723 \[gr-qc\]](https://arxiv.org/abs/2501.11723).
- [4] A. M. Green and B. J. Kavanagh, “Primordial black holes as a dark matter candidate,” *Journal of Physics G: Nuclear and Particle Physics* **48** no. 4, (Feb, 2021) 043001. <http://dx.doi.org/10.1088/1361-6471/abc534>.
- [5] Y. Kahn, B. R. Safdi, and J. Thaler, “Broadband and resonant approaches to axion dark matter detection,” *Physical Review Letters* **117** no. 14, (Sep, 2016) . <https://doi.org/10.1103/PhysRevLett.117.141801>.
- [6] C. P. Salemi, J. W. Foster, *et al.*, “Search for low-mass axion dark matter with abracadabra-10 cm,” *Phys. Rev. Lett.* **127** (Aug, 2021) 081801. <https://link.aps.org/doi/10.1103/PhysRevLett.127.081801>.
- [7] R. T. Co, F. D’Eramo, and L. J. Hall, “Supersymmetric axion grand unified theories and their predictions,” *Phys. Rev. D* **94** (Oct, 2016) 075001. <https://link.aps.org/doi/10.1103/PhysRevD.94.075001>.
- [8] M. Tegmark, A. Aguirre, M. J. Rees, and F. Wilczek, “Dimensionless constants, cosmology, and other dark matters,” *Phys. Rev. D* **73** (Jan, 2006) 023505. <https://link.aps.org/doi/10.1103/PhysRevD.73.023505>.
- [9] P. Sikivie, N. Sullivan, and D. B. Tanner, “Proposal for axion dark matter detection using an *lc* circuit,” *Phys. Rev. Lett.* **112** (Mar, 2014) 131301. <https://link.aps.org/doi/10.1103/PhysRevLett.112.131301>.
- [10] Y. Kahn, B. R. Safdi, and J. Thaler, “Broadband and resonant approaches to axion dark matter detection,” *Phys. Rev. Lett.* **117** (Sep, 2016) 141801. <https://link.aps.org/doi/10.1103/PhysRevLett.117.141801>.
- [11] P. Sikivie, “Invisible axion search methods,” *Reviews of Modern Physics* **93** no. 1, (Feb., 2021) . <http://dx.doi.org/10.1103/RevModPhys.93.015004>.
- [12] P. Sikivie, “Detection rates for “invisible”-axion searches,” *Phys. Rev. D* **32** (Dec, 1985) 2988–2991. <https://link.aps.org/doi/10.1103/PhysRevD.32.2988>.
- [13] P. Sikivie, “Experimental tests of the “invisible” axion,” *Phys. Rev. Lett.* **51** (Oct, 1983) 1415–1417. <https://link.aps.org/doi/10.1103/PhysRevLett.51.1415>.
- [14] L. Krauss, J. Moody, F. Wilczek, and D. E. Morris, “Calculations for cosmic axion detection,” *Phys. Rev. Lett.* **55** (Oct, 1985) 1797–1800. <https://link.aps.org/doi/10.1103/PhysRevLett.55.1797>.
- [15] ADMX Collaboration, C. Goodman *et al.*, “ADMX Axion Dark Matter Bounds around 3.3 μeV with Dine-Fischler-Srednicki-Zhitnitsky Discovery Ability,” *Phys. Rev. Lett.* **134** no. 11, (2025) 111002, [arXiv:2408.15227 \[hep-ex\]](https://arxiv.org/abs/2408.15227).
- [16] HAYSTAC Collaboration, X. Bai *et al.*, “Dark Matter Axion Search with HAYSTAC Phase II,” *Phys. Rev. Lett.* **134** no. 15, (2025) 151006, [arXiv:2409.08998 \[hep-ex\]](https://arxiv.org/abs/2409.08998).
- [17] J. Kim *et al.*, “Near-Quantum-Noise Axion Dark Matter Search at CAPP around 9.5 μeV ,” *Phys. Rev. Lett.* **130** no. 9, (2023) 091602, [arXiv:2207.13597 \[hep-ex\]](https://arxiv.org/abs/2207.13597).
- [18] C. B. Adams *et al.*, “Axion Dark Matter,” in *Snowmass 2021*. 3, 2022. [arXiv:2203.14923 \[hep-ex\]](https://arxiv.org/abs/2203.14923).
- [19] A. V. Gramolin, D. Aybas, D. Johnson, J. Adam, and A. O. Sushkov, “Search for axion-like dark matter with ferromagnets,” *Nature Physics* **17** no. 1, (Aug., 2020) 79–84. <http://dx.doi.org/10.1038/s41567-020-1006-6>.
- [20] L. Brouwer, S. Chaudhuri, *et al.*, “Projected sensitivity of dmradio-m3: A search for the qcd axion below 1 uev,” *Physical Review D* **106** no. 10, (Nov., 2022) . <http://dx.doi.org/10.1103/PhysRevD.106.103008>.
- [21] *Status of DMRadio-50L and DMRadio-m³*. 2022. [arXiv:2210.07215 \[hep-ex\]](https://arxiv.org/abs/2210.07215). <https://arxiv.org/abs/2210.07215>.
- [22] D. Collaboration, A. AlShirawi, *et al.*, “Electromagnetic modeling and science reach of dmradio-m³.” 2023. <https://arxiv.org/abs/2302.14084>.
- [23] L. Brouwer, S. Chaudhuri, *et al.*, “Proposal for a definitive search for gut-scale qcd axions,” *Physical Review D* **106** no. 11, (Dec., 2022) . <http://dx.doi.org/10.1103/PhysRevD.106.112003>.
- [24] M. E. Gertsenshtein., “Wave resonance of light and gravitational waves,” *Sov. Phys. JETP*, *14:84* (1962) .
- [25] D. Boccaletti, V. D. Sabbata, P. Fortini, and C. Gualdi, “Conversion of photons into gravitons and vice versa in a static electromagnetic field,” *Il Nuovo Cimento B (1965-1970)* **70** no. 129, (1970) .

- <https://doi.org/10.1007/BF02710177>.
- [26] G. Raffelt and L. Stodolsky, “Mixing of the photon with low-mass particles,” *Phys. Rev. D* **37** (Mar, 1988) 1237–1249. <https://link.aps.org/doi/10.1103/PhysRevD.37.1237>.
- [27] B. T. McAllister, M. Goryachev, J. Bourhill, E. N. Ivanov, and M. E. Tobar, “Broadband Axion Dark Matter Haloscopes via Electric Sensing,” (3, 2018), [arXiv:1803.07755](https://arxiv.org/abs/1803.07755) [[physics.ins-det](https://arxiv.org/abs/1803.07755)].
- [28] M. E. Tobar, B. T. McAllister, and M. Goryachev, “Modified Axion Electrodynamics as Impressed Electromagnetic Sources Through Oscillating Background Polarization and Magnetization,” *Phys. Dark Univ.* **26** (2019) 100339, [arXiv:1809.01654](https://arxiv.org/abs/1809.01654) [[hep-ph](https://arxiv.org/abs/1809.01654)].
- [29] J. Ouellet and Z. Bogorad, “Solutions to Axion Electrodynamics in Various Geometries,” *Phys. Rev. D* **99** no. 5, (2019) 055010, [arXiv:1809.10709](https://arxiv.org/abs/1809.10709) [[hep-ph](https://arxiv.org/abs/1809.10709)].
- [30] V. Domcke, C. Garcia-Cely, and N. L. Rodd, “Novel search for high-frequency gravitational waves with low-mass axion haloscopes,” *Phys. Rev. Lett.* **129** (Jul, 2022) 041101. <https://link.aps.org/doi/10.1103/PhysRevLett.129.041101>.
- [31] A. Berlin, D. Blas, R. Tito D’Agnolo, S. A. R. Ellis, R. Harnik, Y. Kahn, and J. Schütte-Engel, “Detecting high-frequency gravitational waves with microwave cavities,” *Phys. Rev. D* **105** no. 11, (2022) 116011, [arXiv:2112.11465](https://arxiv.org/abs/2112.11465) [[hep-ph](https://arxiv.org/abs/2112.11465)].
- [32] V. Domcke, C. Garcia-Cely, S. M. Lee, and N. L. Rodd, “Symmetries and selection rules: Optimising axion haloscopes for gravitational wave searches.” 2024.
- [33] A. Berlin, D. Blas, R. Tito D’Agnolo, S. A. R. Ellis, R. Harnik, Y. Kahn, J. Schütte-Engel, and M. Wentzel, “Electromagnetic cavities as mechanical bars for gravitational waves,” *Phys. Rev. D* **108** no. 8, (2023) 084058, [arXiv:2303.01518](https://arxiv.org/abs/2303.01518) [[hep-ph](https://arxiv.org/abs/2303.01518)].
- [34] V. Domcke, S. A. R. Ellis, and N. L. Rodd, “Magnets are Weber Bar Gravitational Wave Detectors,” [arXiv:2408.01483](https://arxiv.org/abs/2408.01483) [[hep-ph](https://arxiv.org/abs/2408.01483)].
- [35] J. L. Ouellet, C. P. Salemi, *et al.*, “First results from abracadabra-10 cm: A search for sub- μeV axion dark matter,” *Phys. Rev. Lett.* **122** (Mar, 2019) 121802. <https://link.aps.org/doi/10.1103/PhysRevLett.122.121802>.
- [36] J. L. Ouellet, C. P. Salemi, *et al.*, “Design and implementation of the ABRACADABRA-10 cm axion dark matter search,” *Physical Review D* **99** no. 5, (Mar, 2019) . <https://doi.org/10.1103/PhysRevD.99.052012>.
- [37] <https://www.alazartech.com/>.
- [38] J. W. Foster, M. Kongsore, C. Dessert, Y. Park, N. L. Rodd, K. Cranmer, and B. R. Safdi, “Deep Search for Decaying Dark Matter with XMM-Newton Blank-Sky Observations,” *Phys. Rev. Lett.* **127** no. 5, (2021) 051101, [arXiv:2102.02207](https://arxiv.org/abs/2102.02207) [[astro-ph.CO](https://arxiv.org/abs/2102.02207)].
- [39] T. D. P. Edwards, K. W. K. Wong, K. K. H. Lam, A. Coogan, D. Foreman-Mackey, M. Isi, and A. Zimmerman, “ripple: Differentiable and hardware-accelerated waveforms for gravitational wave data analysis.” 2023.
- [40] J. W. Foster, Y. Kahn, R. Nguyen, N. L. Rodd, and B. R. Safdi, “Dark Matter Interferometry,” *Phys. Rev. D* **103** no. 7, (2021) 076018, [arXiv:2009.14201](https://arxiv.org/abs/2009.14201) [[hep-ph](https://arxiv.org/abs/2009.14201)].
- [41] S. Ambikasaran, D. Foreman-Mackey, L. Greengard, D. W. Hogg, and M. O’Neil, “Fast Direct Methods for Gaussian Processes,” *IEEE Transactions on Pattern Analysis and Machine Intelligence* **38** (June, 2015) 252, [arXiv:1403.6015](https://arxiv.org/abs/1403.6015) [[math.NA](https://arxiv.org/abs/1403.6015)].
- [42] H. Dembinski and P. O. et al., “scikit-hep/iminuit.” Dec, 2020. <https://doi.org/10.5281/zenodo.3949207>.
- [43] G. Cowan, K. Cranmer, E. Gross, and O. Vitells, “Asymptotic formulae for likelihood-based tests of new physics,” *Eur. Phys. J. C* **71** (2011) 1554, [arXiv:1007.1727](https://arxiv.org/abs/1007.1727) [[physics.data-an](https://arxiv.org/abs/1007.1727)]. [Erratum: *Eur.Phys.J.C* 73, 2501 (2013)].
- [44] M. Frate, K. Cranmer, S. Kalia, A. Vandenberg-Rodes, and D. Whiteson, “Modeling Smooth Backgrounds and Generic Localized Signals with Gaussian Processes,” [arXiv:1709.05681](https://arxiv.org/abs/1709.05681) [[physics.data-an](https://arxiv.org/abs/1709.05681)].
- [45] G. Cowan, K. Cranmer, E. Gross, and O. Vitells, “Power-Constrained Limits,” [arXiv:1105.3166](https://arxiv.org/abs/1105.3166) [[physics.data-an](https://arxiv.org/abs/1105.3166)].

Supplementary Material for high-frequency gravitational wave search with ABRACADABRA-10 cm

Kaliroë M. W. Pappas, Jessica T. Fry, Sabrina Cheng, Arianna Colón Cesaní, Jonathan L. Ouellet, Chiara P. Salemi, Inoela Vital, Lindley Winslow, Valerie Domcke, Sung Mook Lee, Joshua W. Foster, Reyco Henning, Yonatan Kahn, Nicholas L. Rodd, and Benjamin R. Safdi

Strain-Equivalent Noise

Finding the SEN experimentally is effectively the inverse process to determining the instruments response to the merger template. For the SEN we start with power on the digitizer from the full data set,¹ then work backwards to convert to strain. Since the data for ABRA-GW was taken in time ($n_{\text{out}}(t)$), we first had to find the PSD of the data on the digitizer. The data was divided into segments, those segments were Fourier transformed ($\tilde{n}_{\text{out}}(f)$), squared and divided by frequency step to get the PSD ($\mathcal{F}_V(f)$), then all the individual PSDs were averaged together ($\bar{\mathcal{F}}_V(f)$). The final $\bar{\mathcal{F}}_V(f)$ was averaged over the total collection time of six days, representing the averaged PSD of the detector output for the full run.

The input to the detector was found by multiplying $\bar{\mathcal{F}}_V(f)$ by the inverse of the transfer function squared which converts flux on the pickup to voltage on the digitizer,

$$\bar{\mathcal{F}}_V(f)[\mathcal{T}^{-1}(f)_{\Phi \rightarrow V}]^2 = \mathcal{F}_\Phi(f). \quad (\text{S1})$$

To get the SEN, we used simulation to convert flux on the pickup loop to strain. Using the equations for effective current from Ref. [32] as input and separating the h^+ and h^\times terms into distinct simulations, we use Eq. (S1) to find either h^+ or h^\times . Since the simulation results for h^+ and h^\times are not equal, the polarizations must be handled separately. When choosing an incident angle to produce the strongest signal, the h^\times term dominates by an order of magnitude for $\theta_h = \phi_h = \pi/2$, with this in mind we choose approximate the SEN for the h^\times term only. With the simulation-based transfer function, we found $\bar{\mathcal{F}}_{\text{strain}_{h^\times}}(f) = S_n(f)/2$. The factor of 2 relating $S_n(f)$ and $\bar{\mathcal{F}}_{\text{strain}_{h^\times}}(f)$ results from us taking a two-sided PSD on the raw data. The resulting values of $\sqrt{S_n}$ as measured by ABRA-GW are shown as the black curve in Fig. 3.

The theoretical estimate for the sensitivity is computed as follows. The GW flux is determine from Eq. (5), taking $\theta_h = \phi_h = \pi/2$. The flux at the SQUID is taken

Merger Parameter	Value
M_1	$0.01 M_\odot$
M_2	$0.01 M_\odot$
Dimensionless spin	0
Time of coalescence	1 ms
Distance to source	100 km
Inclination	0

TABLE S1. Ripple inputs for the merger template.

to be $\Phi_{\text{SQ}} = (1/2)\sqrt{L/2L_p}\Phi_8$, with L and L_p the inductances of the SQUID and pickup loop, respectively. This determines how a GW signal would manifest as a flux in the SQUID; taking the expected SQUID noise we can invert this mapping to compute the SEN, obtaining $\sqrt{S_n} \simeq 2.9 \times 10^{-9} \text{ Hz}^{-1/2} (f/1 \text{ MHz})^{-2}$, as shown in Fig. 3. We note that this estimate is optimistic: as discussed in Ref. [32], Eq. (5) overestimates the true GW flux by neglecting the finite height contributions.

Merger Signal

All parameters used to generate the merger signal were chosen to maximize the strain in the merger within our frequency window (10 kHz to 3 MHz) and are listed in Table S1. The ripple code base [39] was used to generate the waveforms of the two polarizations of strain ($h^+(\omega)$ and $h^\times(\omega)$) for the merger. Ripple outputs the waveforms as separate polarization arrays in frequency space, which we generate from 1 Hz to 5 MHz. The arrays could in principle be generated from 10 kHz to 5 MHz if we intended to stay in the frequency domain, however the transition to the time domain requires either the full frequency spectrum or a very carefully taken FFT with zero-padded arrays. We transform the arrays output from Ripple to the detector (mV on the digitizer) in the frequency domain before adding them together and taking an inverse FFT and dividing by Δt to get to the time domain. Transformations could be made in the time domain where they would be convolutions instead of multiplications, but this process is both more computationally expensive and careful consideration is needed to perform linear and not circular convolutions.

The transfer function used to convert the strain output from ripple to voltage on the digitizer is in two parts: the first relies on finding the induced flux on the pickup using the analytic form of the effective current from Ref. [32] and COMSOL simulation, and the second part converts

¹ We take the case where there is no HFGW signal for the full data set without losing our ability to claim discovery by using the fact that the signals we look for are transient and lasting $\mathcal{O}(1 \mu\text{s})$. To find the SEN we rfft the data and average over the span of data collection, any transient signal we might be looking for would be averaged to zero and we lack the sensitivity to search for a stochastic signal with only one detector.

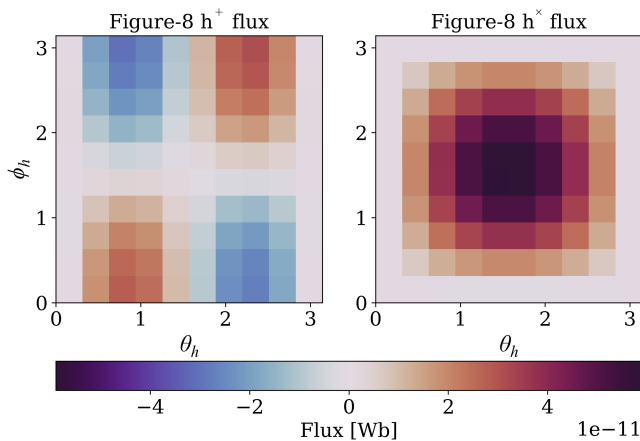


FIG. S1. Each square in the plots is the magnitude of the pickup-loop flux for a given pair of angles. Results are shown for flux calculated over the figure-8 area for $h^\times = 0$, $h^+ = 10^{-4}$ (left) and $h^\times = 10^{-4}$, $h^+ = 0$ (right).

from flux on the pickup to voltage on the ADC and is found from the calibrations.

The full function for the effective current can be found later in the SM, terms up to ω^2 were input to COMSOL as the external current density. The flux through the pickup as a result of the effective current was found by integrating over the surface of the pickup. The effective current for the h^+ and h^\times polarization terms were simulated separately. By testing different values of the strain polarizations, we ensured that the scaling with strain was linear and additive in terms of the two polarizations. To simplify the COMSOL inputs, terms which were constant and consistent across the different components of the effective current were accounted for post-simulation. The flux on the pickup is found to be

$$\Phi_{\text{pickup}} = \frac{1}{\mu_0} \times h^{+/\times}(\omega) \times \omega^2 \times \text{COMSOL}, \quad (\text{S2})$$

where here μ_0 is the permeability of free space, the $h^{+/\times}(\omega)$ terms represent the waveforms for the h^+ and h^\times components of the incoming wave and “COMSOL” is the output from the simulation.

As a result of our goal to create and run our analysis with one template, we chose only one angle for the incoming wave, which was $\pi/2$ for both ϕ_h and θ_h . This angle was chosen to maximize the h^\times component, since the COMSOL results for h^\times were on average an order of magnitude larger. Figure S1 shows the COMSOL flux results for each polarization for incoming angles from 0 to π in θ_h and from 0 to 2π in ϕ_h . In an analogy to the axion search, the conversion of strain to flux on the pickup for the HFGW search includes similar information to the axion geometric coupling term \mathcal{G}_V , which connects the axion current to the current on the pickup.

After finding the flux on the pickup from COMSOL, the gain resulting from the calibration of the HFGW

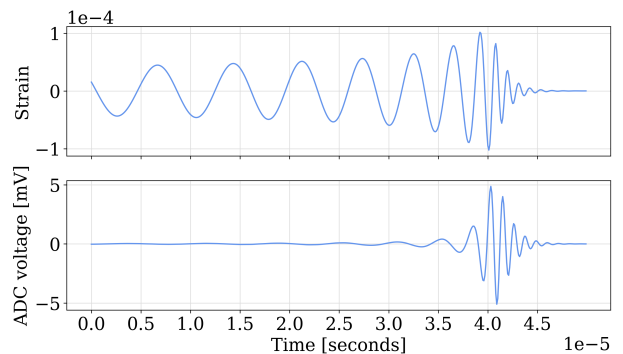


FIG. S2. Signal of a $0.01 M_\odot$ equal mass merger at 100 km distance with the parameters from Table S1. Top: strain from h^+ and h^\times polarizations added together, band-pass filtered and an irfft taken. Bottom: transformed h^+ and h^\times polarizations to the detector frame, band-pass filtered and an irfft taken.

pickup loop with the HFGW calibration loop were used to convert to mV on the digitizer,

$$\Phi_{\text{pickup}} \times \mathcal{T}(f)_{\Phi_{\text{pickup}} \rightarrow V_{\text{ADC}}} = V_{\text{ADC}}. \quad (\text{S3})$$

The transfer function for flux on pickup to voltage on ADC, $\mathcal{T}(f)_{\Phi_{\text{pickup}} \rightarrow V_{\text{ADC}}}$, is found from Eq. (S1) of Ref. [6] dividing the total gain, $V_{\text{ADC}}/V_{\text{Sig}}$, by $\Phi_p/I_C \times I_C/V_{\text{Sig}}$, the mutual inductance between the pickup loop and calibration loop, and the attenuation and current conversion between the signal generator and calibration loop. The results for the two polarizations were then added, an irfft was performed, and the waveforms were band-pass filtered from 10 kHz to 3 MHz. Figure S2 shows the difference between a waveform which was only band-pass filtered in units of strain and one that had the transfer functions applied with units of mV.

In an effort to save computation time, we originally further down-sampled the template, stopping when we could still resolve the template. We determined that we could down-sample by three and still resolve the signal, but two produced a smoother template. However, since the portion of the signal we are using is only $30 \mu\text{s}$ long, resolution gained by using the full signal outweighs the computational benefits. This benefit was determined by running the Gaussian process algorithm on a segment of test data with a known signal injected and different amounts of down-sampling on the template and data, the algorithm recovered the signal with the least amount of uncertainty with no down-sampling.

Gaussian Process Modeling

Gaussian Process Modeling (GPM) treats the data as a realization of a potentially nontrivial gaussian process, allowing for analyses to replace inference of parametrically specified background models with inference of hyperparameters that specify the kernel of the gaussian process

covariance. In choosing a kernel, we aim to specify a covariance model which is sufficiently flexible to accurately model smooth backgrounds while not being so flexible that it can also generate signal-like features, which would result in degraded detection sensitivity.

For the analysis presented here, in which we search for GW-like signals as they appear in the time-domain of ADC voltage measurements, we choose the exponential sine-squared kernel,

$$K(t, t' | A_{\text{GP}}, \Gamma, P) = A_{\text{GP}} \exp \left(-\Gamma \sin^2 \left[\frac{\pi}{P} |t - t'| \right] \right). \quad (\text{S4})$$

This kernel specifies a covariance between time-domain measurement of the background process at times t and t' , in terms of the covariance normalization A_{GP} , the covariance scale Γ , and the covariance periodicity P . This is a safe choice of kernel as our interest is in inspiral signals which chirp, realizing time-varying periodicity, while the period of our kernel is stationary and only allowed to take values in a range which is mismatched with respect to characteristic signal frequencies. We make use of the python package `George`[41] to implement our GPM.

To perform our analysis, we consider detector data at \mathbf{s} , where \mathbf{s}_i is the ADC voltage at time t_i , and a signal template $\mathbf{h}(d)$ where $\mathbf{h}_i(d)$ is the prediction for the GW signal at time t_i for an inspiral at a distance d from the detector. We then construct the signal-subtracted data $\mathbf{r} = \mathbf{s} - \mathbf{h}$, which we assume are described by a mean-zero gaussian process with covariance $\mathbf{K}_{ij} = K(t_i, t_j | A_{\text{GP}}, \Gamma, P)$. We then calculate the marginalized likelihood of the signal-subtracted data by

$$\ln p(\mathbf{r}|d) = -\frac{1}{2} \mathbf{r}^T \mathbf{K}^{-1} \mathbf{r} - \frac{1}{2} \ln \det \mathbf{K} - \frac{n}{2} \ln(2\pi). \quad (\text{S5})$$

where n is the length of data vector \mathbf{r} . Note that this likelihood also depends on the GPM hyperparameters, which we have omitted from equation above for compactness.

We treat this likelihood following standard frequentist techniques, performing maximum likelihood inference to estimate the distance of a putative binary inspiral as well as the GPM hyperparameters. We perform these likelihood maximizations using the `iminuit` code package [42]. In addition, we determine 90% central confidence intervals associated with a 5th percentile lower limit and 95th percentile upper limit assuming the asymptotic limit from the Fisher information matrix calculated about the maximum likelihood estimate [43]. We also define a test statistic, denoted TS, for an inspiral at distance d given by

$$\text{TS}(d) = -2 \ln \frac{p(\mathbf{r}|d)}{p(\mathbf{r}|\hat{d})} \quad (\text{S6})$$

where \hat{d} is the maximum likelihood estimate of the signal distance and the probability of the data given the inspiral distance are independently maximized for both

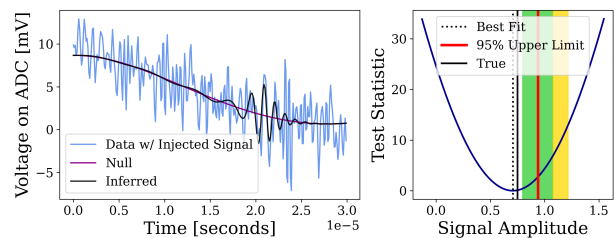


FIG. S3. Gaussian Process Modeling run on a single segment of data. Left: the “Null” line was produced by the GPM fit to the background and the “Inferred” line is that background plus the signal with the best-fit amplitude found from the regression. Right: The profile likelihood is shown in dark-blue with a minimum at the best-fit amplitude value. 90% confidence with one-sigma bounds (green) and two-sigma bound (yellow).

\hat{d} and d . This test statistic, in the asymptotic limit, can be interpreted as a χ^2 -distributed quantity, see [38, 44]. We also determine 16th percentile lower limits following the power-constrained limit procedure [45].

As an example of our analysis, in Fig. S3, we show the GPM analysis and TS minimization on one segment of data with an injected signal at a distance of 133 km, which corresponds to 100 km/ A where A is the amplitude of the signal and has a value of 0.75 for this injection. We repeat this procedure, sliding the time of the inspiral event to inspect the data for a signal which appears over a finite time interval.

Binary exclusion

To determine the exclusion rate on PBHs, we performed the GPM analysis on each windowed segment of data. For each of these segments we collected a best-fit amplitude and an error on that amplitude, which were used to create the 90% CL for each segment. We found the largest 90% CL in these results, which gave us the distance of 46.03 km quoted in the main body of this paper. All other segments excluded further distances, meaning the 90% CL on that distance is the most conservative result over that interval. Figure S4 shows the distribution in 90% CLs over the windowed segments, along with the fraction of segments which exclude a given distance.

Data Stability and Variance

Over the course of data taking in December of 2023 we measured the variance on the HFGW data. As can be seen in Fig. S5, the RMS of the variance is tightly confined between roughly 20.8 to 22.1, with a vague pattern of noise increasing during the night. We define “night” for winter in Cambridge MA as the time range from around 17:00 to 7:00. The slight increase in variance during the night is likely the resulting from generators turning on in

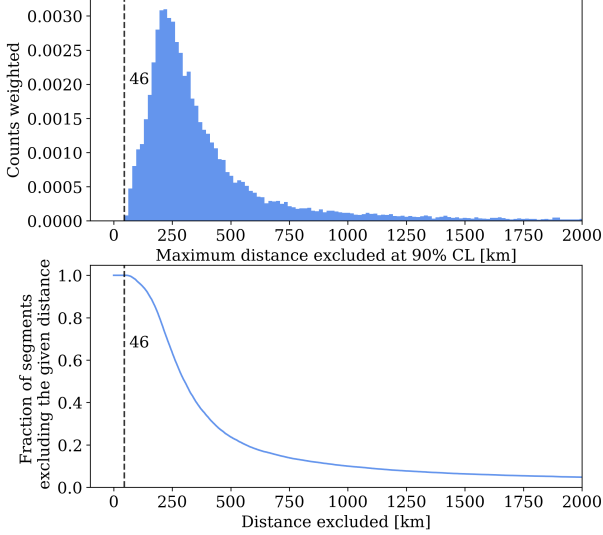


FIG. S4. Top: weighted distribution of 90% CL results for the GPM analysis over 10 ms of data. Bottom: fraction of windowed segments which exclude a given amplitude to at least a 90% CL.

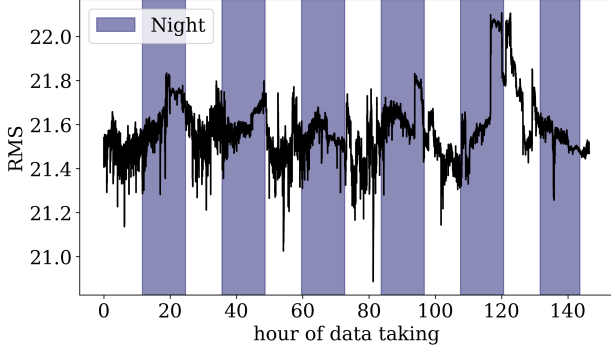


FIG. S5. Root-mean-square of the variance of the ABRA-GW HFGW data. The portions of data-taking that occurred during the night are marked in purple.

the building or other environmental effects.

Effective Current in Toroidal Magnet

Here we provide the full form of the GW current at the leading order of $\omega^2 L^2$ appropriate for a toroidal magnet, as originally determined in Ref. [32] including a higher order. The results are divided into three parts: one proportional to $[\Theta(R + a - \rho) - \Theta(R - \rho)][\Theta(H - 2z) + \Theta(H + 2z)]$ describing the volume current, one proportional to $\delta(R + a - \rho) - \delta(R - \rho)$ describing the current on the inside and outside of the volume and one proportional to $\delta(H - 2z) - \delta(H + 2z)$ describing the top and bottom of the magnet. Note the dimensions of the magnet are $H = 120$ mm and $R = a = 30$ mm. In the following, we use the shorthand s_θ and c_θ for $\sin\theta$ and $\cos\theta$. We further take $\phi_h = 0$, but ϕ_h can be restored by taking $\phi \rightarrow \phi - \phi_h$, which was done when inputting the equations into COMSOL.

$$\begin{aligned}
 j_\rho e^{i\omega t} = & \frac{B_{\max} R \omega^2}{\rho} [\Theta(R + a - \rho) - \Theta(R - \rho)] [\Theta(H - 2z) + \Theta(H + 2z)] \\
 & \times \left[\frac{1}{12\sqrt{2}} h^+ \left\{ 2z(3 + c_{2\theta_h}) c_{2\phi} + 6z s_{\theta_h}^2 - \rho c_\phi s_{2\theta_h} \right\} + \frac{1}{6\sqrt{2}} h^\times (8z c_{\theta_h} c_\phi - \rho s_{\theta_h}) s_\phi \right] \\
 & - \frac{B_{\max} R \omega^2}{\rho} [\Theta(R + a - \rho) - \Theta(R - \rho)] [\delta(H - 2z) - \delta(H + 2z)] \\
 & \times \left[\frac{1}{12\sqrt{2}} h^+ \left\{ (z^2 + 2\rho^2)(3 + c_{2\theta_h}) c_{2\phi} + 2z s_{\theta_h} (-4\rho c_{\theta_h} c_\phi + 3z s_{\theta_h}) \right\} + \frac{1}{3\sqrt{2}} h^\times \left\{ (z^2 + 2\rho^2) c_{\theta_h} s_{2\phi} - 2z \rho s_{\theta_h} s_\phi \right\} \right]
 \end{aligned} \tag{S7}$$

$$\begin{aligned}
j_\phi e^{i\omega t} &= \frac{B_{\max} R \omega^2}{\rho} [\Theta(R + a - \rho) - \Theta(R - \rho)] [\Theta(H - 2z) + \Theta(H + 2z)] \\
&\times \left[-\frac{1}{6\sqrt{2}} h^+ \{z(3 + c_{2\theta_h})c_\phi + \rho s_{2\theta_h}\} s_\phi + \frac{1}{3\sqrt{2}} h^\times (z c_{\theta_h} c_{2\phi} + \rho c_\phi s_{\theta_h}) \right] \\
&+ B_{\max} R \omega^2 [\delta(R + a - \rho) - \delta(R - \rho)] [\Theta(H - 2z) + \Theta(H + 2z)] \\
&\times \left[\frac{1}{12\sqrt{2}} h^+ \{z(3 + c_{2\theta_h})c_\phi + \rho s_{2\theta_h}\} s_\phi - \frac{1}{6\sqrt{2}} h^\times (z c_{\theta_h} c_{2\phi} + \rho c_\phi s_{\theta_h}) \right] \\
&+ \frac{B_{\max} R z \omega^2}{\rho} [\delta(R + a - \rho) - \delta(R - \rho)] [\delta(H - 2z) - \delta(H + 2z)] \\
&\times \left[\frac{1}{12\sqrt{2}} h^+ \{2\rho s_{2\theta_h} s_\phi + z(3 + c_{2\theta_h})s_{2\phi}\} - \frac{1}{3\sqrt{2}} h^\times (z c_{\theta_h} c_{2\phi} + \rho c_\phi s_{\theta_h}) \right]
\end{aligned} \tag{S8}$$

$$\begin{aligned}
j_z e^{i\omega t} &= \frac{B_{\max} R \omega^2}{\rho^2} [\Theta(R + a - \rho) - \Theta(R - \rho)] [\Theta(H - 2z) + \Theta(H + 2z)] \\
&\times \left[\frac{1}{12\sqrt{2}} h^+ \left\{ (z^2 - 2\rho^2)(3 + c_{2\theta_h})c_{2\phi} + 3z\rho c_\phi s_{2\theta_h} \right\} + \frac{1}{6\sqrt{2}} h^\times \left\{ 4(z^2 - 2\rho^2)c_{\theta_h} c_\phi + 3z\rho s_{\theta_h} \right\} s_\phi \right] \\
&+ \frac{B_{\max} R \omega^2}{\rho} [\delta(R + a - \rho) - \delta(R - \rho)] [\Theta(H - 2z) + \Theta(H + 2z)] \\
&\times \left[\frac{1}{24\sqrt{2}} h^+ \left\{ (z^2 + 2\rho^2)(3 + c_{2\theta_h})c_{2\phi} + 2z s_{\theta_h} (-4\rho c_{\theta_h} c_\phi + 3z s_{\theta_h}) \right\} + \frac{1}{3\sqrt{2}} h^\times \left\{ (z^2 + 2\rho^2)c_{\theta_h} c_\phi - z\rho s_{\theta_h} \right\} s_\phi \right]
\end{aligned} \tag{S9}$$
